

# Towards a robust detection of viscous and turbulent flow regions using unsupervised Machine Learning

Kheir-Eddine Otmani<sup>a,\*</sup>, Gerasimos Ntoukas<sup>a</sup>, Esteban Ferrer<sup>a,b</sup>

<sup>a</sup>*ETSIAE-UPM-School of Aeronautics, Universidad Politécnica de Madrid, Plaza Cardenal Cisneros 3, E-28040 Madrid, Spain*

<sup>b</sup>*Center for Computational Simulation, Universidad Politécnica de Madrid, Campus de Montegancedo, Boadilla del Monte, 28660 Madrid, Spain*

---

## Abstract

We propose an invariant feature space for the detection of viscous dominated and turbulent regions (i.e., boundary layers and wakes). The developed methodology uses the principal invariants of the strain and rotational rate tensors as input to an unsupervised Machine Learning Gaussian mixture model. The selected feature space is independent of the coordinate frame used to generate the processed data, as it relies on the principal invariants of strain and rotational rate, which are Galilean invariants. This methodology allows us to identify two distinct flow regions: a viscous dominated, rotational region (boundary layer and wake region) and an inviscid, irrotational region (outer flow region). We test the methodology on a laminar and a turbulent (using Large Eddy Simulation) case for flows past a circular cylinder at  $Re = 40$  and  $Re = 3900$ . The simulations have been conducted using a high-order nodal Discontinuous Galerkin Spectral Element Method (DGSEM). The results obtained are analysed to show that Gaussian mixture clustering provides an effective identification method of viscous dominated and rotational regions in the flow. We also include comparisons with traditional sensors to show that the proposed clustering does not depend on the selection of an arbitrary threshold, as required when using traditional sensors.

*Keywords:* Computational Fluid Dynamics, Machine Learning, Gaussian Mixture, High-Order Discontinuous Galerkin

---

## Contents

<b>1</b>	<b>Introduction</b>	<b>2</b>
<b>2</b>	<b>Methodology</b>	<b>4</b>
2.1	Gaussian mixture . . . . .	4
2.2	Traditional sensors . . . . .	5
2.3	High order discontinuous Galerkin solver . . . . .	6
2.4	Numerical Simulations . . . . .	6

---

\*Corresponding author

*Email address:* `otmani.kheir-eddine@alumnos.upm.es` (Kheir-Eddine Otmani)

2.4.1	Numerical simulation at $Re = 40$	6
2.4.2	Numerical simulation at $Re = 3900$	6
<b>3</b>	<b>Results</b>	<b>8</b>
3.1	Cylinder flow at $Re=40$	8
3.2	Cylinder flow at $Re=3900$	8
3.3	A note on the relevance of the invariants	12
3.3.1	Feature space $(\mathbf{Q}_S, \mathbf{R}_S)$	14
3.3.2	Feature space $(\mathbf{Q}_S, \mathbf{Q}_\Omega)$	14
3.3.3	Feature space $(\mathbf{R}_S, \mathbf{Q}_\Omega)$	17
<b>4</b>	<b>Conclusions</b>	<b>19</b>

## 1. Introduction

The large amount of data generated by computational fluid dynamics (CFD) simulations has led scientists towards the use of new Machine Learning (ML) techniques to help perform post-processing analysis, such as the detection of flow regions or flow features [13, 6]. These regions or features can subsequently be used to identify physical mechanisms or construct surrogate models. Alternatively, the regions can be used from a numerical perspective to increase local resolution (e.g. refine the mesh or increase the polynomial order in high-order methods) or to apply different sets of equations in each region (e.g. near wall turbulent region and inviscid far field). Overall, there is great potential in using Machine Learning techniques to identify flow regions, which is the main topic of this work. To detect regions using machine learning, one can use classification or clustering [40]. Both allow for the grouping of data by creating clusters of points/elements with similar properties/values. The fundamental problem to be solved is the determination of the boundary of these nuclei, which will differentiate the classified/clustered data. Classification algorithms (e.g., Logistic Regression, K-Nearest Neighbours, Decision Tree, Support Vector Machines) belong to the supervised learning category and require predetermined labelled data sets to guide and train the machine learning algorithm. Clustering (e.g., Gaussian mixture models, K-means, Mini-Batch K-Means, Mean Shift, Spectral Clustering) [5], is an unsupervised learning method that does not require pre-sampled data to cluster regions and can automatically discover grouping in data. In this work, we select clustering as it requires minimum supervision.

The combination of fluid dynamics with neural networks and deep learning is an emerging field [6, 42]. Recently, deep neural networks have been used to build surrogates of closure turbulence models [19, 41, 47, 14, 24], to accelerate numerical simulations (e.g., [2, 22, 23]) and to solve partial differential equations (e.g., [38, 31, 43, 32]).

More relevant to this work is the recent use of ML for flow region identification in [18] as a supervised ML classification (supervised learning) method was used to identify turbulent and non-turbulent regions in a flow past a circular cylinder at a variety of turbulent Reynolds numbers. The authors used a variety of inputs (e.g., kinetic energy, vorticity) and invariants of strain rate and vortical tensors to train an extreme gradient boosting XGBoost classifier. In the context of the identification of turbulent/non-turbulent regions, [45] used

self-organising map clustering [16] to distinguish the turbulent boundary layer from non-turbulent regions in a transitional flow. These results were encouraging and motivated our work, which is based on the clustering method. The main advantage of using ML to perform flow region classification or clustering is that the methodology does not require the choice of any threshold and can treat multiple inputs. On the contrary, classic detectors heavily dependent on the selected threshold, as first pointed out by [45], and corroborated in section 3.

When treating Reynolds Averaged Navier-Stokes (RANS) simulations, [35, 17] showed that various viscous sensors could be used as input to a clustering ML framework. The aim was to detect the boundary layer and wake regions for turbulent flow past a NACA 0012 airfoil. The methodology combined viscous sensors to perform a soft clustering of the given data. The results showed that the ML clustering outperformed the classic viscous sensors used to identify the flow regions in RANS. In [7], unsupervised learning techniques were proposed to identify the dominant physical processes for different flow scenarios and in [8] the authors trained a neural network to classify different types of vortex wakes. Authors in [4] used supervised learning and convolution neural networks [1] to locate shock positions within a discontinuous Galerkin solver and used the output of this framework for shock capturing applications.

In relation to the parameter space for the clustering method, [19] showed in the context of Reynolds averaged turbulence modelling that using Galilean invariants to train the ML model is beneficial since it ensures independence between the coordinate inertial frame used to generate the data and the predictions made by the ML model.

In this work, we aim at distinguishing not only turbulent/non-turbulent regions but also at detecting viscous dominated regions from outer inviscid regions. To do so, we construct a robust flow feature space (i.e., useful for subsonic laminar and turbulent regimes) and allow for two clustering regions. The first is a viscous and turbulent dominated region and the second is an inviscid outer region. Note that this is different from [45], where turbulent and laminar regions are distinct clusters. We aim to distinguish near wall and wake regions from inviscid/potential flow regions (far from objects in the flow). We propose to use a data-driven clustering approach, the Gaussian mixture clustering. The selection of the feature space, which is fed into the Gaussian mixture clustering is critical and has to carry the physical information needed to distinguish the boundary layer and wake regions from the outer flow region, see details in section 2. Such a space is constrained to maintain the Galilean invariance. To test our proposed methodology, we conduct numerical experiments on a laminar and a turbulent flow past a circular cylinder.

The reason for having only two regions (laminar/turbulent and inviscid) is that an extension of this work will be to locally increase the resolution in these regions (e.g. refine the mesh or increase the polynomial order in high-order methods) to improve the accuracy in our simulations. Alternatively, these regions can be used to compute drag, as proposed for RANS in [35, 17].

The rest of this work is structured as follows. First, we introduce the ML methodology and the selected flow features to train the ML model in section 2 and denote the details of the numerical experiments for the laminar and turbulent (LES) cases. In section 3, we present the results along with the analysis of the clustering and the resulting flow regions.

## 2. Methodology

We propose a ML framework to detect viscous and turbulent (i.e., highly rotational) flow regions. The methodology is based on the assumption that the boundary and wake regions are characterized by non-negligible viscous dissipation and high vorticity/rotation in the flow field while the outer flow region is inviscid and irrotational (e.g., potential flow). Note that this will be verified a-posteriori in our analysis, as presented in section 3. We construct a robust flow feature space to be used as input to an unsupervised ML framework. Intuitively, this feature space must be independent of the coordinate frame used to generate the data and for this reason we propose to use the principal invariants of strain rate and rotational rate tensors. The two strain rate tensor invariants are defined as

$$Q_S = \frac{1}{2}(tr(\mathbf{S})^2 - tr(\mathbf{S}^2)) \ ; \ R_S = -\frac{1}{3}det(\mathbf{S}),$$

where  $\mathbf{S}$  is the strain rate tensor defined as:  $\mathbf{S} = \frac{1}{2}(\mathbf{J} + \mathbf{J}^T)$  and  $\mathbf{J} = \nabla\mathbf{U}$  is the gradient tensor of the velocity field  $\mathbf{U}$ .  $Q_S$  is proportional to the local viscous dissipation rate  $\epsilon = -4\mu Q_S$ , with  $\mu$  denoting the fluid viscosity [46].  $R_S$  is relevant as it relates to regions of high viscous dissipation. Positive values of  $R_S$  indicate high rates of strain production, while negative values of  $R_S$  indicate the destruction of the strain product [9]. The rotational tensor  $\mathbf{\Omega}$  has only one invariant defined as

$$Q_\Omega = -\frac{1}{2}tr(\mathbf{\Omega}^2),$$

where  $\mathbf{\Omega} = \frac{1}{2}(\mathbf{J} - \mathbf{J}^T)$ .  $Q_\Omega$  is related to the enstrophy density  $\xi$  [46] defined by  $\xi = \int_D |\boldsymbol{\omega}|^2 dD$ , where  $\boldsymbol{\omega}$  is the flow vorticity in the domain  $D$ . Enstrophy can be associated to high turbulent dissipation rate and can be used to detect turbulent regions. High values of  $Q_\Omega$  identify rotational and turbulent regions in the flow field. Using these quantities as input, we propose the feature space

$$E = (Q_S, R_S, Q_\Omega).$$

This feature space  $E$  is used as input to the Gaussian mixture model to cluster the data into two different regions. The boundary layer and wake regions (viscous and turbulent dominated) and the outer flow region (inviscid and irrotational). The Gaussian mixture model is preferred over simpler clustering (e.g. K-means) for its superiority in discovering complex non-linear patterns in the data [28]. We will test this feature space with two different regimes (laminar  $Re = 40$  and turbulent  $Re = 3900$ ) to verify that we can distinguish laminar/turbulent dominated regions from outer inviscid regions. In section 3, we demonstrate why these 3 invariants are sufficient to detect the two regions of interest. Furthermore, we will showcase that it is not advantageous to reduce the feature space as all three invariants are necessary.

### 2.1. Gaussian mixture

Clustering is the process of categorising data into different groups. This is essentially performed by discovering underlying patterns within the given data [36]. It should be noted

that clustering is an unsupervised learning approach which can separate data without the necessity of specifying a ground truth, unlike in supervised approaches, which require expert guidance by providing a set of labels to guide the learning process.

The model adopted in this work is the Gaussian Mixture Model (GMM) [5]. Under the hypothesis that the data are generated from a mixture of Gaussian distributions, GMM clusters the data into different subpopulations, each following a Gaussian distribution. The algorithm estimates the mean and variance of each normal distribution iteratively using the Expectation-Maximization (EM) method [10] to provide the optimal estimation of these parameters. The EM method consists of two main steps. The expectation step (E-step), in which the conditional expectation of the data is computed, given the available samples. This is done essentially to fill in the missing values in the given data. The second step is the maximisation step (M-step), where the maximisation of the conditional expectation, computed previously in the E-step, is used to update the mean and variance of the normal distributions. These two steps are repeated iteratively until no significant changes are observed in the estimated parameters. Namely, we use a tolerance of  $10^{-4}$  to stop the algorithm with regard to the difference of the conditional probabilities from the previous iteration [25].

For clustering purposes, GMM considers each Gaussian distribution as a cluster and assigns each data sample to a cluster based on a membership probability. The number of Gaussian distributions  $N$  should be provided prior to the model training process. In this work, we select  $N = 2$  as we aim to detect two flow regions, a viscous-dominated, rotational region (boundary layer and wake region) and an inviscid irrotational region (outer flow region). Several clustering algorithms are available in open source libraries such as *scikit-learn* [29] which offers different choices based on different unsupervised learning frameworks. Our implementation uses the Gaussian mixture class in the *scikit-learn* Python library [29].

## 2.2. Traditional sensors

In section 3, the results from our proposed clustering method will be compared against two classic sensors used for the classification of flow regions, the dissipation of kinetic energy and the eddy viscosity sensor.

The first sensor under consideration is the dissipation of kinetic energy, which is defined as

$$\frac{F_{\Phi}}{\mu} = 2 \left( \left( \frac{\partial u}{\partial x} \right)^2 + \left( \frac{\partial v}{\partial y} \right)^2 + \left( \frac{\partial w}{\partial z} \right)^2 \right) + \left( \frac{\partial v}{\partial x} + \frac{\partial u}{\partial y} \right)^2 + \left( \frac{\partial w}{\partial y} + \frac{\partial v}{\partial z} \right)^2 + \left( \frac{\partial u}{\partial z} + \frac{\partial w}{\partial x} \right)^2 - \frac{2}{3} \left( \frac{\partial u}{\partial x} + \frac{\partial v}{\partial y} + \frac{\partial w}{\partial z} \right)^2,$$

where  $u, v, w$  are the three velocity components [37].

We also select a turbulent sensor: the eddy viscosity sensor [26] defined as

$$F_{\mu_t} = \frac{\mu + \mu_t}{\mu},$$

where  $\mu$  and  $\mu_t$  are the physical and turbulent viscosities accordingly. Note that this sensor detects turbulent regions ( $F_{\mu_t} > 1$  if  $\mu_t > 0$ ) and is unable to detect laminar regions within the boundary layer and the wake ( regions where  $\mu_t \rightarrow 0$  ) [17].

To detect the boundary layer and wake regions using the aforementioned sensors, it is necessary to choose a threshold parameter  $K$ . Regions where  $F_\Phi > K$  or  $F_{\mu_t} > K$  will be considered as turbulent regions (boundary layer and wake regions), whereas regions where  $F_\Phi \leq K$  or  $F_{\mu_t} \leq K$  will be considered as an inviscid, irrotational region (outer region). The identification of a suitable value for the threshold parameter  $K$  is arbitrary and non-trivial [17] and is often determined through a trial and error process. We will show that our proposed clustering does not require any specification of a threshold parameter.

### 2.3. High order discontinuous Galerkin solver

The numerical simulations have been carried out using the HORSES3D numerical framework, see [11]. The compressible Navier-Stokes equations have been discretised using a high-order Discontinuous Galerkin Spectral Element Method (DGSEM) [34]. The computational domain is tessellated into non-overlapping curvilinear hexahedral elements to approximate complex geometries. The solution within each element is represented with an arbitrary polynomial approximation order and can be discontinuous across different elements. The discontinuities between elements are treated through the use of suitable fluxes. In this work we use the Roe Riemann solver [33] for the convective fluxes and BR1 for the viscous fluxes [3]. The multiphysics environment of HORSES3D also offers the option of using several subgrid turbulence models. We use the Smagorinsky LES model for the turbulent cylinder at  $Re = 3900$  [39]. Time marching is conducted using a low-storage  $3^{rd}$  order explicit Runge-Kutta scheme [44]. In all cases, the Mach number is 0.1 and the flow is considered incompressible. More details for each of the test cases are included in the following sections.

### 2.4. Numerical Simulations

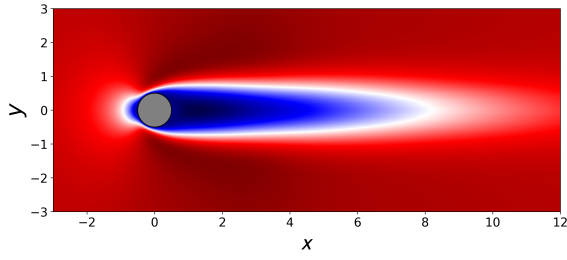
We train the Gaussian mixture algorithm with the data obtained from numerical simulations of the flow past a circular cylinder in two different regimes: a laminar 2D steady flow at  $Re = 40$ , a turbulent 3D flow at  $Re = 3900$ , with a Smagorinsky subgrid closure model.

#### 2.4.1. Numerical simulation at $Re = 40$

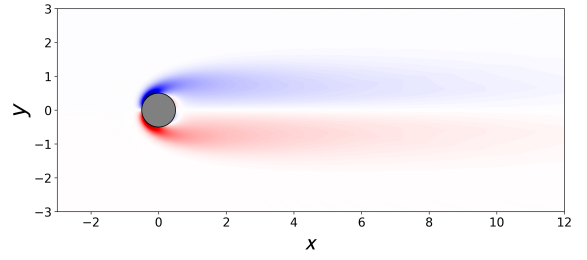
We use a polynomial of order 2 (i.e.,  $3^{rd}$  order accurate) in 53088 hexahedral elements. Our methodology will cluster the degrees of freedom resulting from the high-order discretisation. Therefore, all nodal points provided by the polynomial order within each element will be treated by the clustering technique, with a total of  $53088 \times (P + 1)^3 = 1.43 \times 10^6$  degrees of freedom. Figure 1 presents contours of the magnitude of the stream velocity  $u$  and the spanwise vorticity component  $\omega_z$ .

#### 2.4.2. Numerical simulation at $Re = 3900$

This case has been studied with various numerical frameworks and schemes [12, 21, 27]. The flow has been computed using polynomial order 4 approximation (i.e.,  $5^{th}$  order) with a hexahedral mesh of 20736 elements, as shown in figure 2a. The mesh has been extruded in the spanwise direction as  $L_z/D = \pi$  and subdivided into 16 elements along this direction, with a polynomial of order 4 also used along this direction. In this case, the number of clustered points (degrees of freedom) is  $20736 \times (P + 1)^3 = 2.59 \times 10^6$ . To ensure that aliasing errors are minimised and the method is robust, split form discretization with Pirozzoli averaging has been used [30]. In figure 3, we present a comparison for two different wake statistics quantities against other experimental and numerical results for this case.

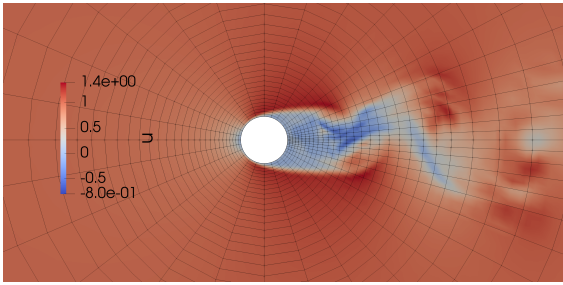


(a) Streamwise velocity magnitude  $u$  for a flow past a cylinder at  $Re = 40$ .

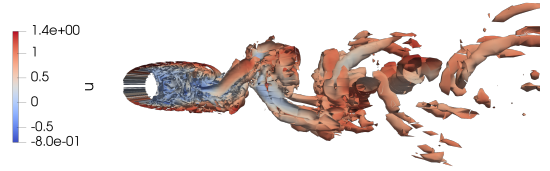


(b) Spanwise vorticity component  $\omega_z$  for a flow past a cylinder at  $Re = 40$ .

Figure 1: Streamwise velocity  $u$  and spanwise vorticity  $\omega_z$  for a flow past a circular cylinder at  $Re = 40$ .

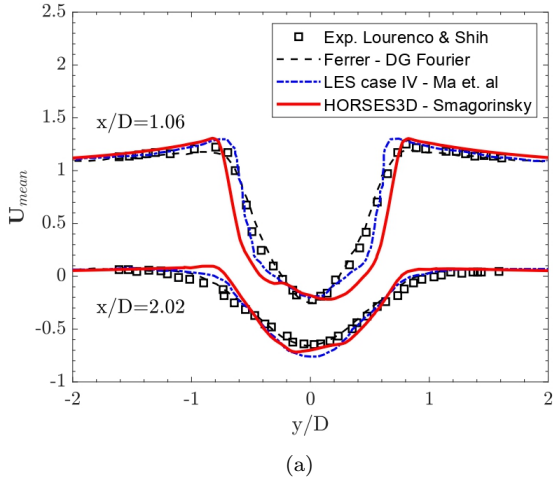


(a) Close-up of the axial velocity  $u$  along the midline and the mesh used for the flow around a cylinder at  $Re=3900$ .

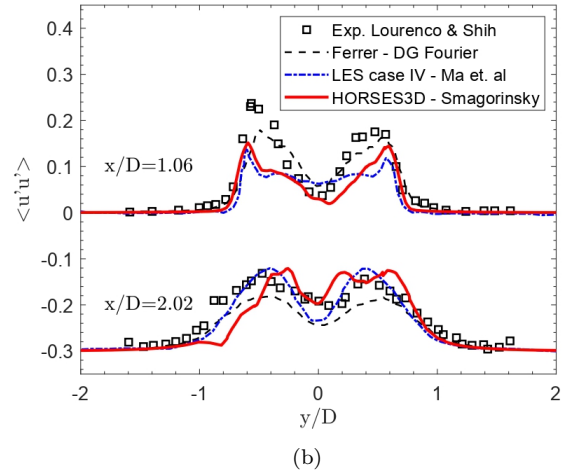


(b) Isosurface of vorticity magnitude  $\|\omega\| = 1$  coloured with the axial velocity  $u$  for a flow past a cylinder at  $Re = 3900$ .

Figure 2: Mesh and vorticity magnitude isosurface  $\|\omega\|$  for the flow past a circular cylinder at  $Re = 3900$ .



(a)



(b)

Figure 3: Mean streamwise velocity  $U_{mean}$  in (3a) and streamwise Reynolds stresses  $\langle u'u' \rangle$  in (3b) downstream of the cylinder at locations  $x/D = 1.06$  and  $x/D = 2.02$  for the flow past a circular cylinder at  $Re = 3900$ . We compare the data from HORSES3D against the data from Ferrer [12], the LES results of Ma et al. [21] and the experimental data from Lourenco and Shih [20].

### 3. Results

In this section, we present the results obtained using the Gaussian mixture algorithm to distinguish the boundary layer and wake region from the outer flow region.

#### 3.1. Cylinder flow at $Re=40$

To validate our methodology, we cluster the data obtained from a numerical simulation at  $Re = 40$  with the setup described in section 2.4. Using the feature space  $E$  as input for the GMM, the detected regions are presented in figure 4d. The results of the GMM approach are compared in figure 4 with the results obtained using the kinetic energy dissipation sensor  $F_\Phi$ , see section 2.2, with different values for the threshold parameter  $K \in [10, 70]$ . As presented in figures 4a, 4b, 4c, the results with the traditional sensor are highly sensitive to the choice of the threshold parameter  $K$  and different values of  $K$  lead to very different regions and misidentify part of the outer region as part of the viscous dominated region. An appropriate choice of  $K$  is challenging and requires a trial and error process, whereas ML clustering is free from selecting any threshold value. Figure 4 shows that our GMM clustering can provide a satisfactory detection of the boundary layer and wake regions.

To further investigate the detected regions by the GMM and quantify the accuracy of the clustering, we present the scatter plots of  $Q_S$ ,  $R_S$  and  $Q_\Omega$  in each clustered region. Figure 5 presents the scatter plots of the invariants of strain and rotational rate tensors maps  $(Q_\Omega, -Q_S)$ ,  $(Q_\Omega, R_S)$  and  $(R_S, -Q_S)$ . It is important to mention that the data presented in the plots are scaled with the maximum of the data in the entire domain. By doing so, we can easily see that if the data are close to one, the degrees of freedom with large values of the invariant are included in the selected region. However, if the degrees of freedom have low values for the scaled invariants, then the region does not contain significant viscous/turbulent effects.

The scatter plot of  $(Q_\Omega, -Q_S)$  in figure 5a shows that high viscous dissipation and vorticity values are concentrated in the clustered region where the boundary layer and wake are included, while viscous dissipation and enstrophy are negligible in the region identified as the outer flow, as the values of  $\frac{-Q_S}{\max(-Q_S)}$  and  $\frac{Q_\Omega}{\max(Q_\Omega)}$  are of order  $O(10^{-4})$  and  $O(10^{-6})$ .

The clustering and scatter plots provide additional information since, as explained in [9], in regions where  $Q_\Omega \approx -Q_S$  the flow is known to have a vortex sheet shape [15] as shown in figure 5a. The scatter plots of  $(Q_\Omega, R_S)$  and  $(R_S, -Q_S)$  in figures 5c and 5e indicate that the detected boundary layer and wake are characterised by high rates of strain production and destruction in the flow field. On the contrary, in the outer flow region no strain production or destruction occurs, as shown in figures 5d and 5f.

#### 3.2. Cylinder flow at $Re=3900$

In the case of the flow past a circular cylinder at  $Re = 3900$  we use the solution field at a time instant after the flow has been fully developed. We perform the clustering using the same feature space  $E$ , see section 2, to challenge its robustness through this turbulent case. We compare our clustering method with the classic eddy viscosity sensor  $F_{\mu_t}$ . The eddy viscosity sensor has been tested with different parameters  $K$  from the interval  $K \in [1.25, 1.75]$ .

The results are presented in figure 6c,6b and 6a for the traditional sensors and 6d for the proposed clustering. The figures show that the GMM clustering can provide similar results to



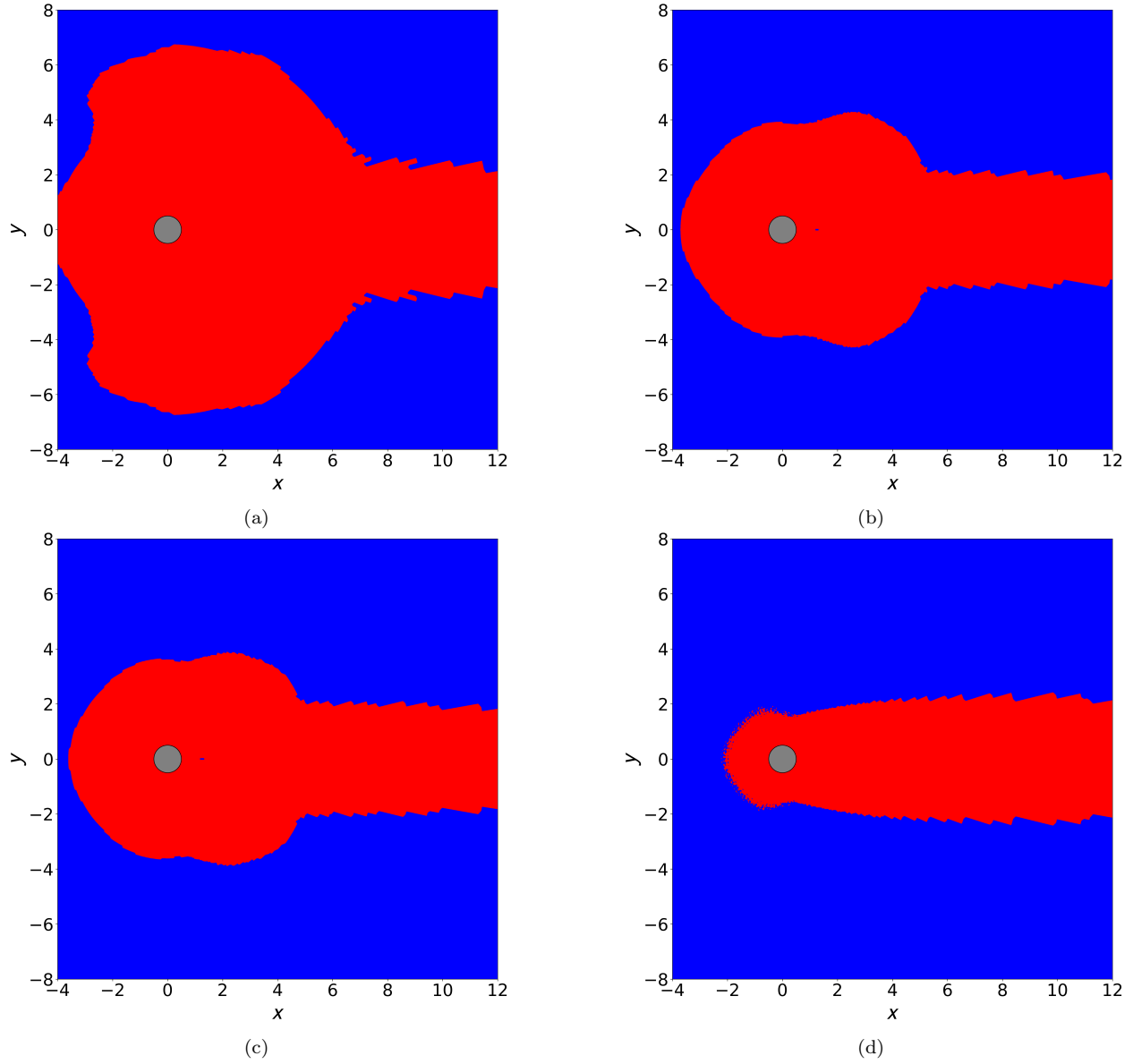
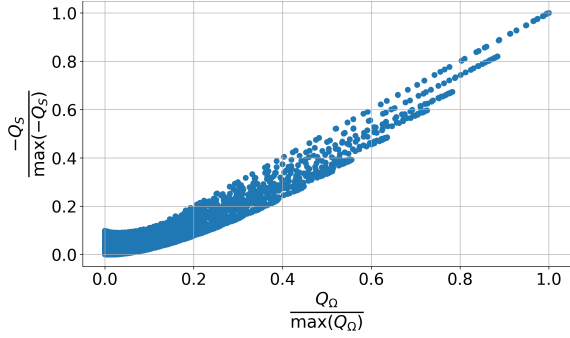
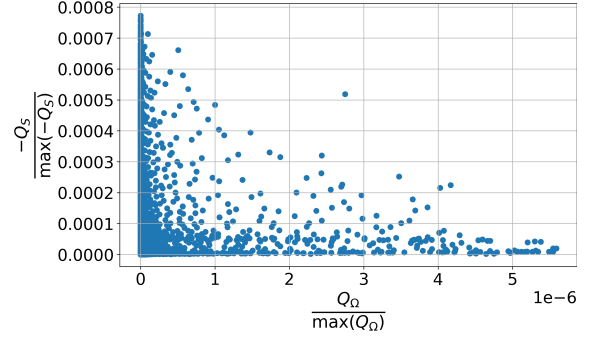


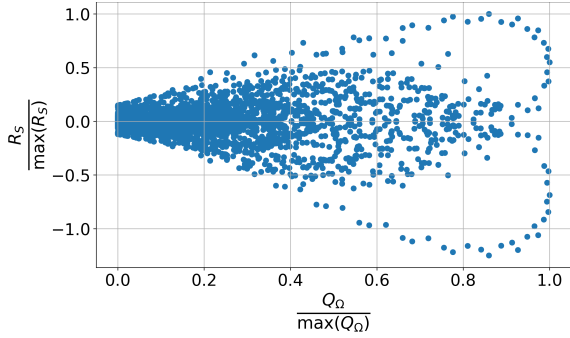
Figure 4: Flow regions detection for flow past a cylinder at  $Re = 40$  using dissipation of kinetic energy sensor  $F_\Phi$ ,  $K = 10$  (4a),  $K = 50$  (4b),  $K = 70$  (4c) and GMM clustering with feature space  $E$ . (4d). **Red**: Boundary layer and wake regions, **Blue**: Outer flow region.



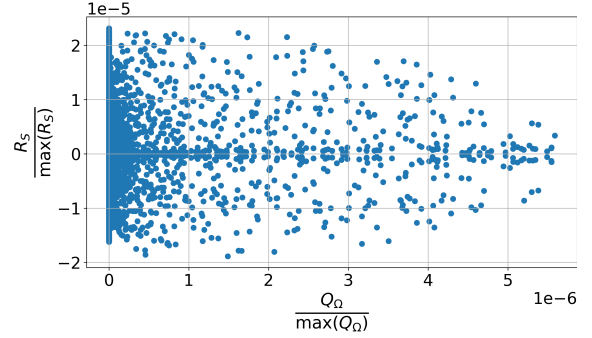
(a)  $(Q_\Omega, -Q_S)$  scatter plot in the detected boundary layer and wake region.



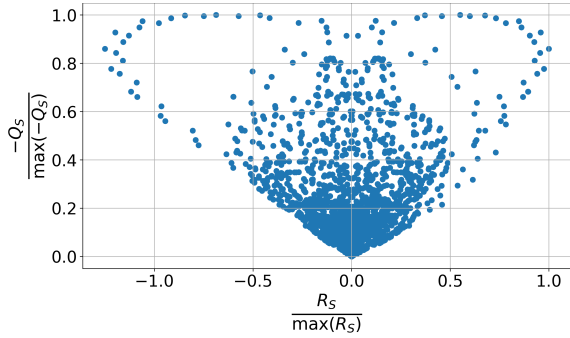
(b)  $(Q_\Omega, -Q_S)$  scatter plot in the detected outer flow region.



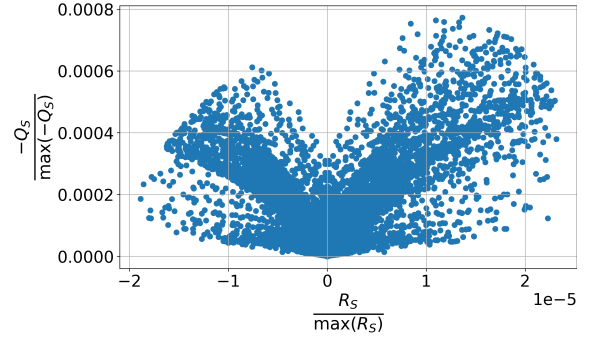
(c)  $(Q_\Omega, R_S)$  scatter plot in the detected boundary layer and wake region.



(d)  $(Q_\Omega, R_S)$  scatter plot in the detected outer flow region.



(e)  $(R_S, -Q_S)$  scatter plot in the detected boundary layer and wake region.



(f)  $(R_S, -Q_S)$  scatter plot in the detected outer flow region.

Figure 5: Scatter plot of  $(Q_\Omega, -Q_S)$ ,  $(Q_\Omega, R_S)$  and  $(R_S, -Q_S)$  in the detected regions by the GMM clustering.

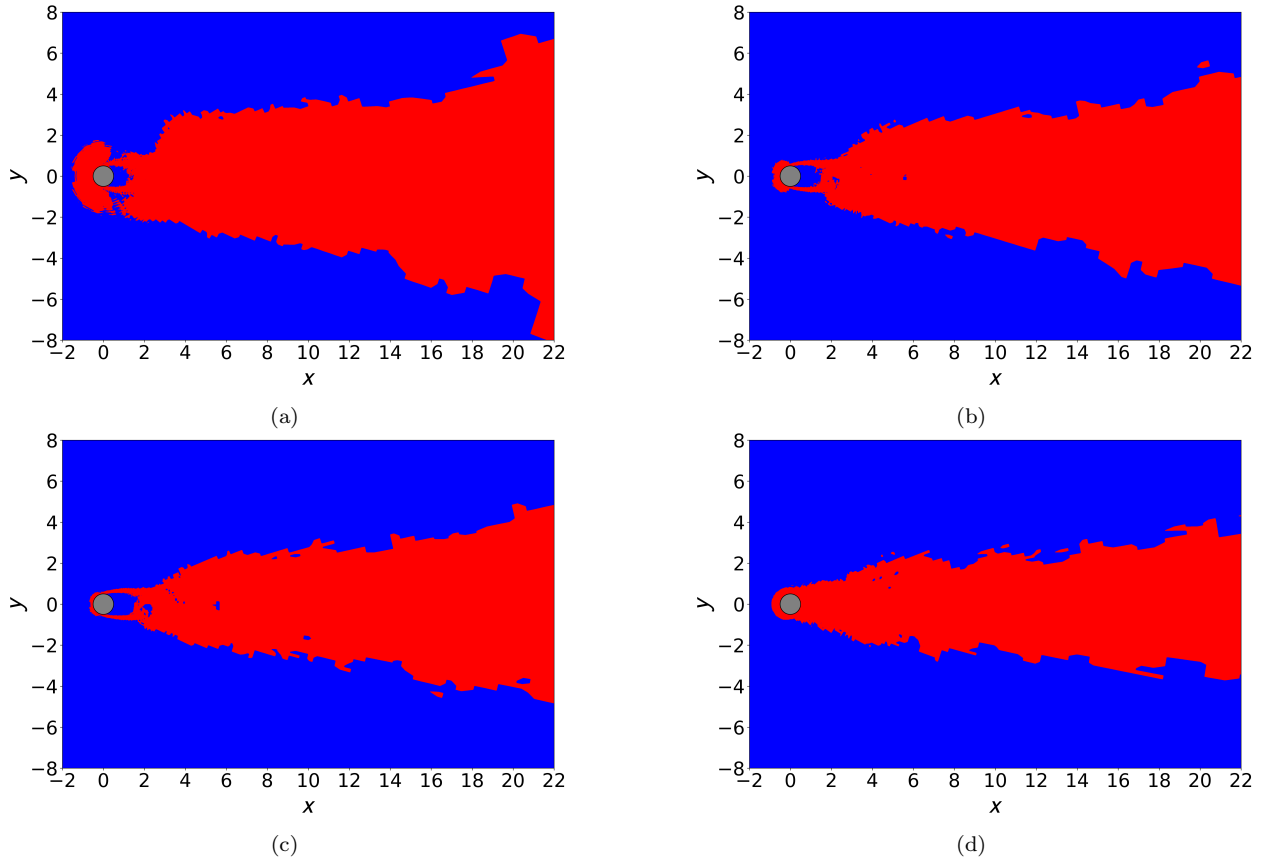


Figure 6: Flow regions detection for flow past a cylinder at  $Re = 3900$  using eddy viscosity sensor  $F_{\mu_t}$ ,  $K = 1.25$  (6a),  $K = 1.5$  (6b),  $K = 1.75$  (6c) and GMM clustering with feature space  $E$ . (6d), Red: Boundary layer and wake regions, Blue: Outer flow region.

the classic sensor (when tuned correctly  $K \sim 1.75$ ). Note that the classic sensor  $F_{\mu_t}$  fails to identify a region in the near wake, close to the back of the cylinder, where there is no turbulent viscosity ( $\mu_t \rightarrow 0$ ). However, this region is dominated by viscous effects and is misidentified by  $F_{\mu_t}$  as being part of the outer region. Our methodology successfully clusters this region into the viscous/turbulent regions. The GMM clustering method, along with the feature space  $E$ , can overcome this issue and detects the viscous-dominated region downstream of the cylinder, as presented in figure 6d, without the need of tuning the threshold of any parameters.

As in the case of the laminar flow, we analyse the scatter plots of the invariants of the strain and rotational rate tensor maps  $(Q_\Omega, -Q_S)$ ,  $(Q_\Omega, R_S)$  and  $(R_S, -Q_S)$  which are presented in figure 7. Again, the plots are scaled with the maximum values of  $Q_\Omega, -Q_S$  and  $R_S$  in the entire flow.

The high values of viscous dissipation and enstrophy are concentrated in the detected boundary layer and wake regions, as shown in figure 7a. In the detected outer flow region, viscous dissipation and enstrophy are negligible, as the values of  $\frac{-Q_S}{\max(-Q_S)}$  and  $\frac{Q_\Omega}{\max(Q_\Omega)}$  are of order  $O(10^{-4})$  and  $O(10^{-7})$ , respectively. In addition, the clustering and scatter plots provide physical insights. Two flow structures can be observed in this case within the detected boundary layer and wake region. Following the results presented in figure 7a, the first region is where  $Q_\Omega = -Q_S$  and is related to the existence of a vortex sheet shape [15]. In the second region, enstrophy is dominant, with high values of  $Q_\Omega$  and negligible values of  $Q_S$ , which can be interpreted as a vortex tube shape [9].

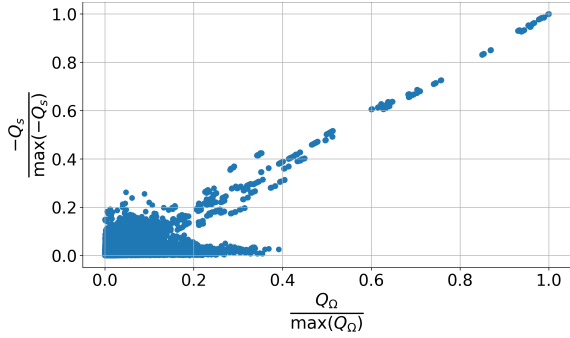
Figures 7c and 7e show that considerable strain production and destruction occur in the detected boundary layer and wake regions. In the detected outer flow region, no clear shapes/features appear as shown in figures 7d and 7f.

We also provide scatter plots for the traditional sensors to show their inadequacy in clustering regions. Figure 8 presents the scatter plot of  $(Q_\Omega, -Q_S)$  in the outer region detected using the eddy viscosity sensor  $F_{\mu_t}$  and the GMM clustering with feature space  $E$ . The threshold parameter  $K$  of the turbulent viscosity sensor  $F_{\mu_t}$  is set to  $K = 1.75$ . The comparison of the scatter plots of the  $(Q_\Omega, -Q_S)$  map shows that the GMM clustering outperforms the traditional sensor.

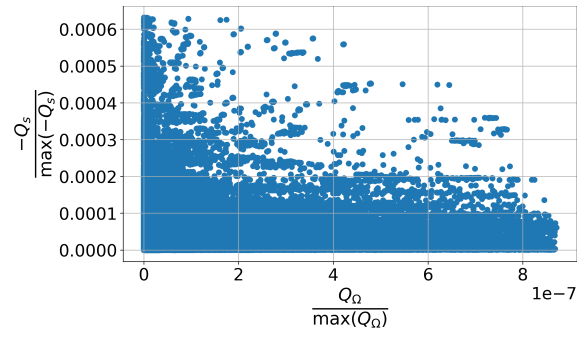
As shown in figures 6a, 6b and 6c,  $F_{\mu_t}$  is unable to cluster regions where  $\mu_t \rightarrow 0$  downstream of the cylinder into the viscous dominated region. This region is characterised by non-negligible viscous dissipation. The scatter plot 8b shows that a relatively high viscous dissipation is present in the region classified as outer flow by  $F_{\mu_t}$  as  $\frac{-Q_S}{\max(-Q_S)}$  reaches values of 0.02. This corresponds to the misidentified regions downstream of the cylinder in figures 6a, 6b and 6c. For GMM clustering with the feature space  $E$ ,  $\frac{-Q_S}{\max(-Q_S)}$  is of the order  $O(10^{-4})$  in the detected outer region. High enstrophy values can also be observed in the outer region detected using  $F_{\mu_t}$  as  $\frac{Q_\Omega}{\max(Q_\Omega)}$  reaches 0.2 compared to the enstrophy values in the outer region detected with GMM clustering where this value is of order  $O(10^{-7})$ , see figure 8a.

### 3.3. A note on the relevance of the invariants

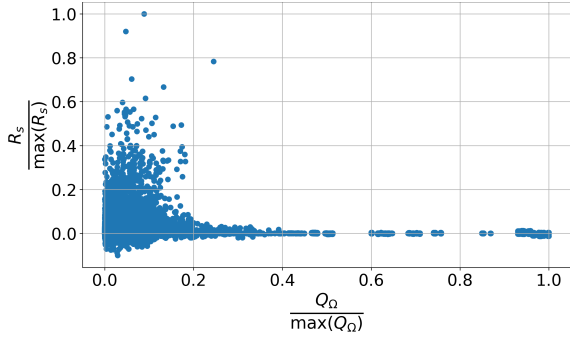
In this section we discuss the relevance of using each of the invariants in the feature space  $E$ . In addition, we will verify that the selected feature space includes the minimum set of variables necessary to detect the boundary layer and wake region, and that when this



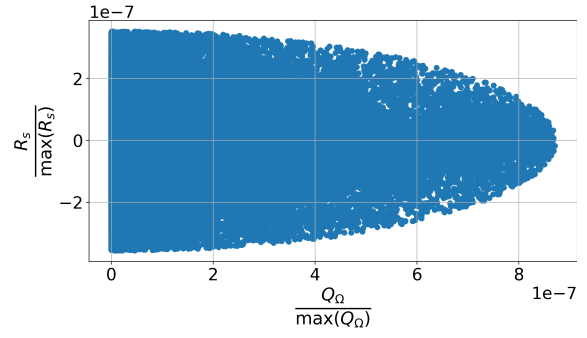
(a)  $(Q_\Omega, -Q_S)$  scatter plot in the detected boundary layer and wake region.



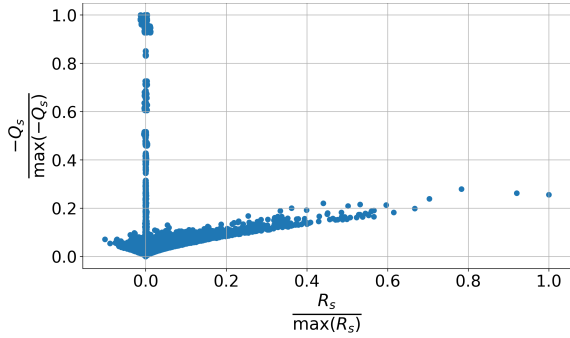
(b)  $(Q_\Omega, -Q_S)$  scatter plot in the detected outer flow region.



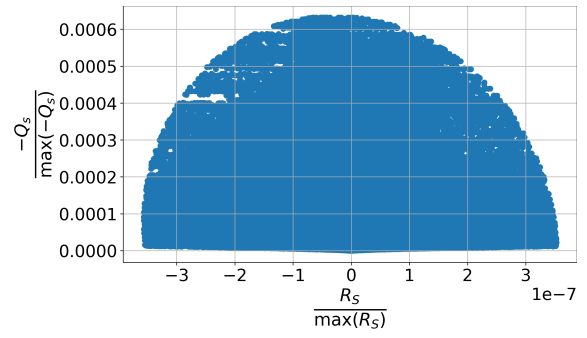
(c)  $(Q_\Omega, R_S)$  scatter plot in the detected boundary layer and wake region.



(d)  $(Q_\Omega, R_S)$  scatter plot in the detected outer flow region.

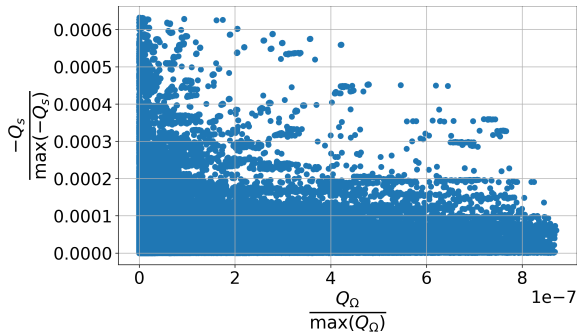


(e)  $(R_S, -Q_S)$  scatter plot in the detected boundary layer and wake region.

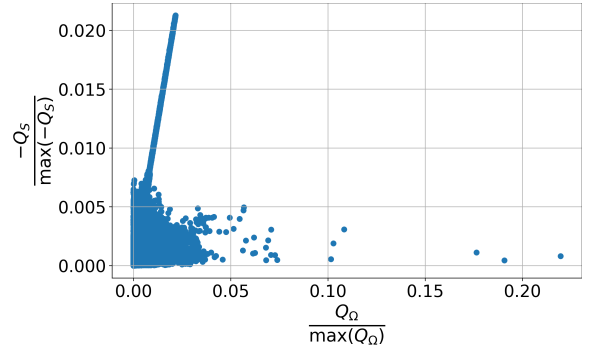


(f)  $(R_S, -Q_S)$  scatter plot in the detected outer flow region.

Figure 7: Scatter plot of  $(Q_\Omega, R_S)$ ,  $(Q_\Omega, -Q_S)$  and  $(R_S, -Q_S)$  in the detected regions by the GMM clustering.



(a)  $(Q_\Omega, -Q_S)$  scatter plot in the detected outer flow region at  $Re = 3900$  with feature space  $E$ .



(b)  $(Q_\Omega, -Q_S)$  scatter plot in the detected outer flow region at  $Re = 3900$  with  $F_{\mu_t}$ .  $K = 1.75$ .

Figure 8:  $(Q_\Omega, -Q_S)$  scatter plot in the detected outer flow region at  $Re = 3900$  with  $F_{\mu_t}$ .  $K = 1.75$  and GMM clustering with feature space  $E$ .

space is reduced (to only two invariants) we cannot capture the correct flow regions. Each one of the invariants in the feature space  $E$  provide specific information about the physical mechanisms and all are deemed to be necessary. To check this hypothesis, we train the GMM clustering with  $(Q_S, R_S)$  or  $(Q_S, Q_\Omega)$  or  $(R_S, Q_\Omega)$  for both Reynolds numbers (laminar and turbulent cases, see section 2.4). The new (reduced space) regions will be compared with the ones obtained when using the original feature space  $E$ .

### 3.3.1. Feature space $(Q_S, R_S)$

The results in figures 5a ( $Re = 40$ ) and 7a ( $Re = 3900$ ) show that there is a strong correlation between  $Q_S$  and  $Q_\Omega$  in the detected boundary layer and wake region due to the presence of vortex sheet structures. Performing the clustering using  $(Q_S, R_S)$ , without considering the effect of  $Q_\Omega$  in the feature space, we retrieve the results illustrated in figure 9.

The results in figure 9 show patches within the wake region that are classified as outer flow region (namely in the turbulent case). This is due to the fact that within the wake, enstrophy dominated regions cannot be identified when  $Q_\Omega$  is excluded from the feature space used to train the GMM. In figure 10, we compare the enstrophy values for the outer flow region when detecting it using  $(Q_S, R_S)$  and when the clustering was performed with the feature space  $E$  for the two test cases under consideration.

In figures 10b and 10d the value of  $\frac{Q_\Omega}{\max(Q_\Omega)}$  reaches 0.015 for  $Re = 40$  and 0.025 for  $Re = 3900$  when using  $(Q_S, R_S)$  for detection. On the contrary, using the feature space  $E$  leads to enstrophy values which are of the order  $O(10^{-6})$ .

### 3.3.2. Feature space $(Q_S, Q_\Omega)$

If we exclude  $R_S$  from the feature space  $E$  and proceed to carry out the clustering with  $(Q_S, Q_\Omega)$ , we retrieve the results presented in figure 11. Part of the wake is identified as an outer flow region in the laminar case as shown in figure 11a. For the turbulent case, the detected wake region is narrower compared to the one detected with feature space  $E$  in figure 6d. To investigate the quality of the detected regions using  $(Q_S, Q_\Omega)$ , we compare the scatter plot of the invariants maps  $(-Q_S, R_S)$  in the detected outer flow regions using the feature space  $E$  and  $(Q_S, Q_\Omega)$ . The results are presented in the scatter plots of figures 12b and 12d. Relatively higher strain production and destruction are detected by GMM in the

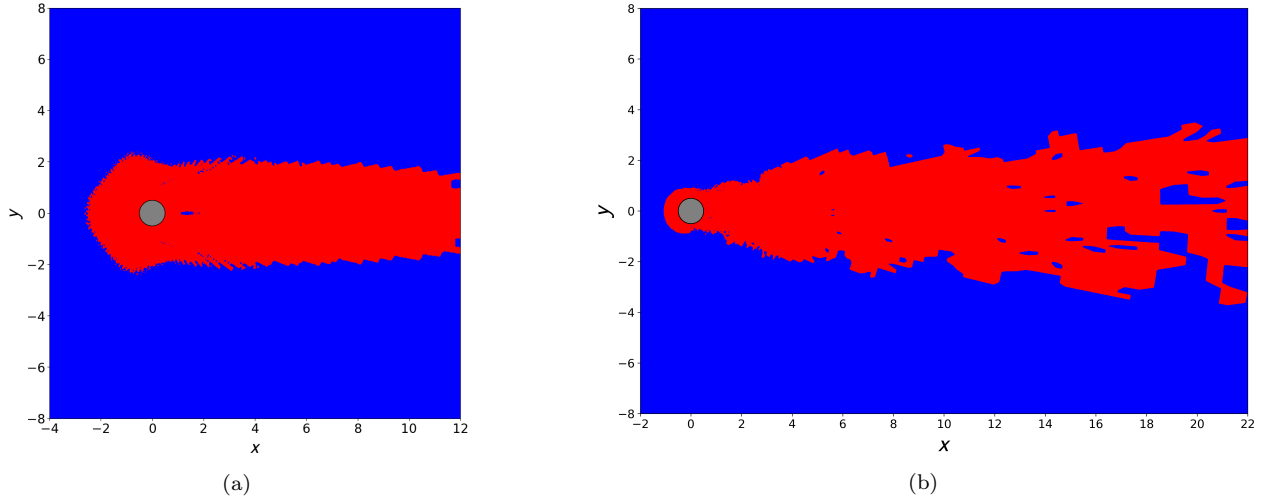


Figure 9: Flow regions detected by GMM for flow past a cylinder at  $Re = 40$ . (9a) and  $Re = 3900$ . (9b) using  $(Q_S, R_S)$ , Red: Boundary layer and wake regions, Blue: Outer flow region.

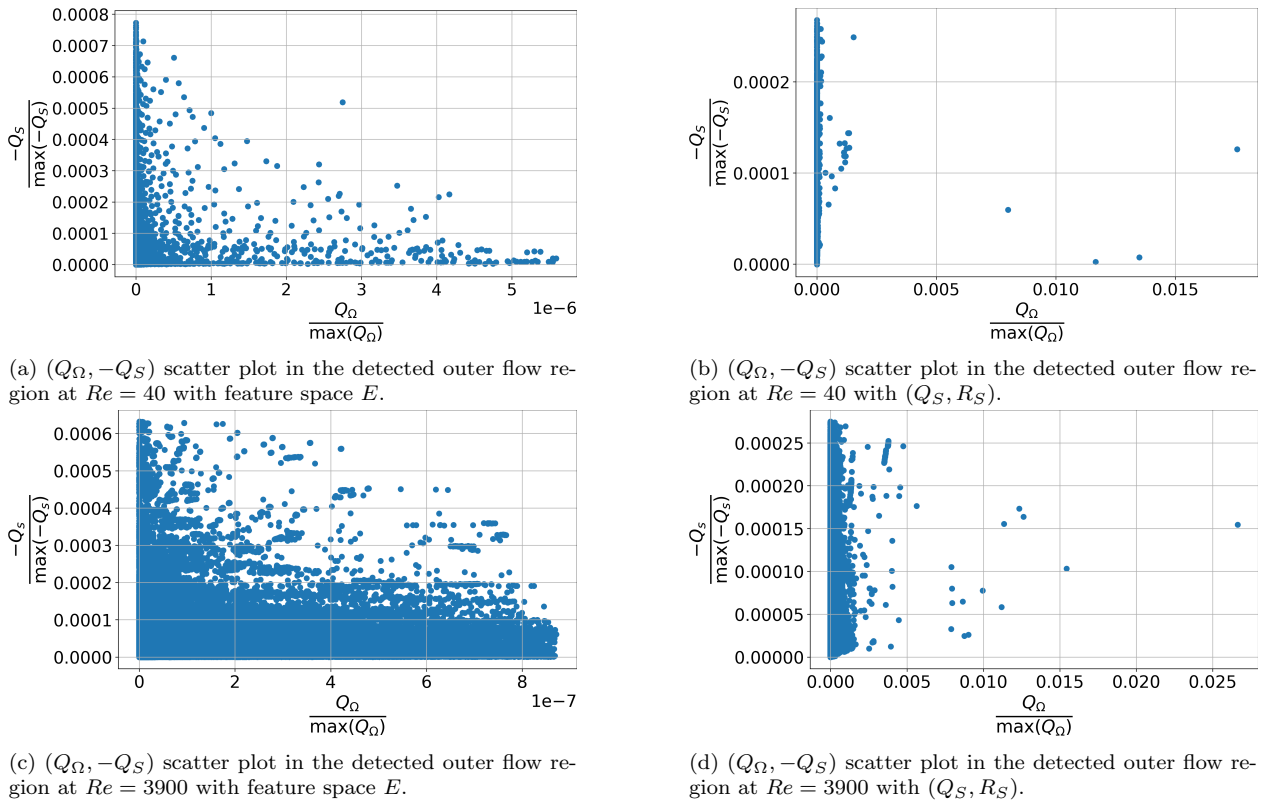


Figure 10:  $(Q_\Omega, -Q_S)$  scatter plot in the detected outer flow region by GMM using the feature space  $E$  and  $(Q_S, R_S)$ .

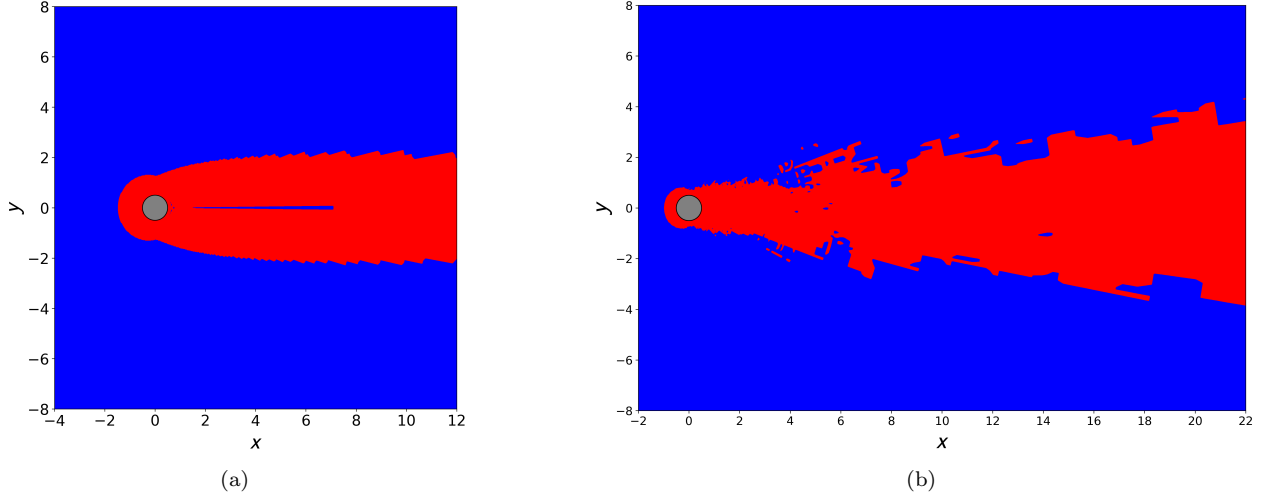
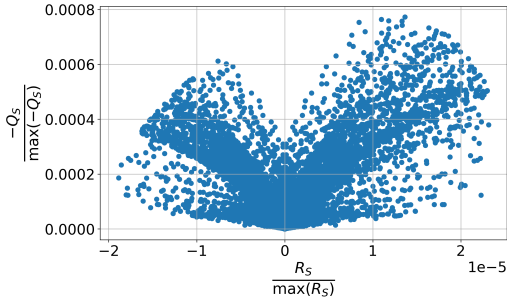
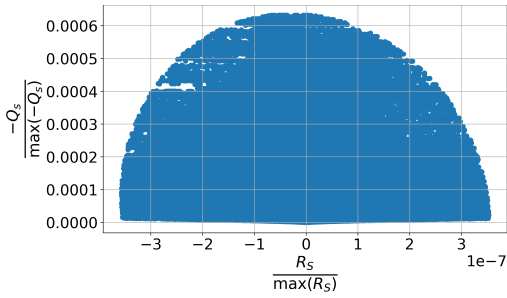


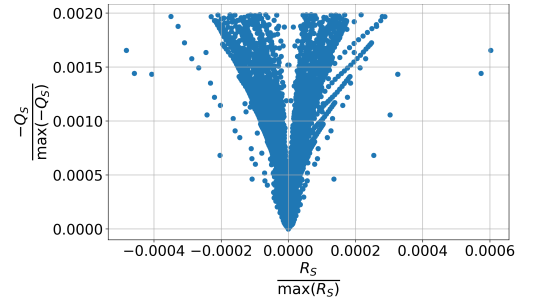
Figure 11: Flow regions detected by GMM for flow past a cylinder at  $Re = 40$ . (11a) and  $Re = 3900$ . (11b) using  $(Q_S, Q_\Omega)$ , **Red**: Boundary layer and wake regions, **Blue**: Outer flow region.



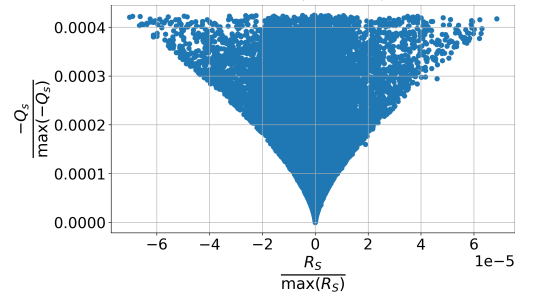
(a)  $(R_S, -Q_S)$  scatter plot in the detected outer flow region at  $Re = 40$  with feature space  $E$ .



(c)  $(R_S, -Q_S)$  scatter plot in the detected outer flow region at  $Re = 3900$  with feature space  $E$ .



(b)  $(R_S, -Q_S)$  scatter plot in the detected outer flow region at  $Re = 40$  with  $(Q_S, Q_\Omega)$ .



(d)  $(R_S, -Q_S)$  scatter plot in the detected outer flow region at  $Re = 3900$  with  $(Q_S, Q_\Omega)$ .

Figure 12:  $(R_S, -Q_S)$  scatter plot in the detected outer flow region by GMM using the feature space  $E$  and  $(Q_S, Q_\Omega)$ .



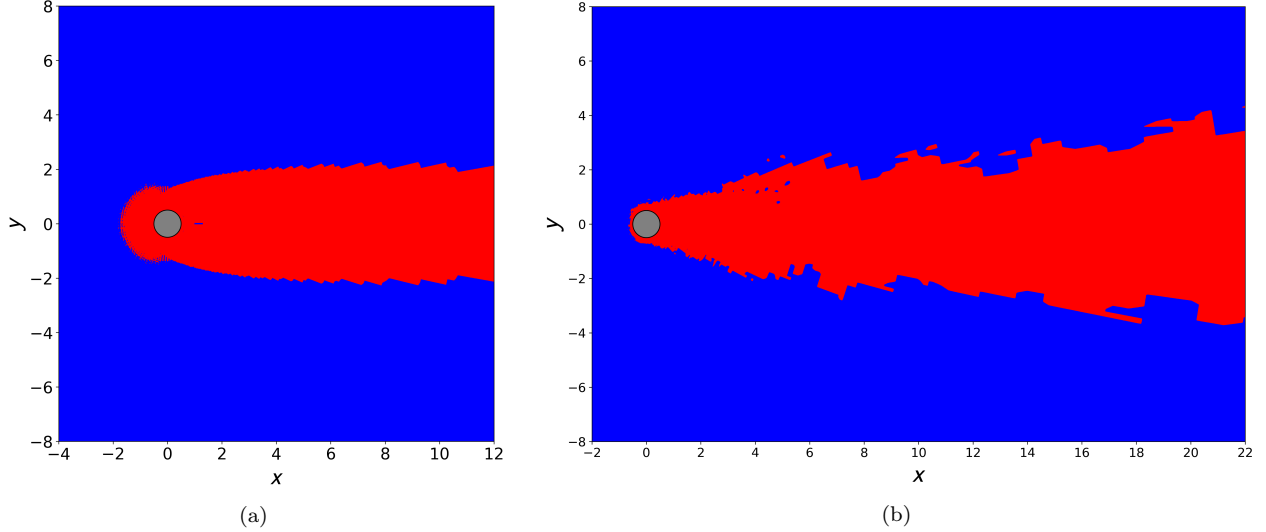


Figure 13: Flow regions detected by GMM for flow past a cylinder at  $Re = 40$ . (11a) and  $Re = 3900$ . (11b) using  $(R_S, Q_\Omega)$ , Red: Boundary layer and wake regions, Blue: Outer flow region.

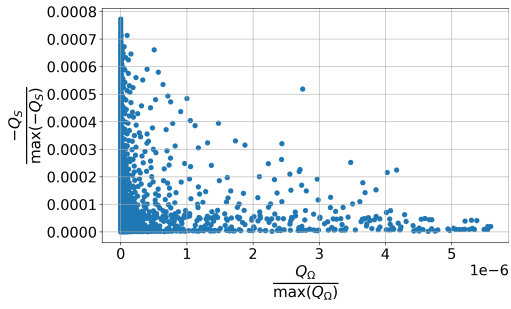
outer region when using  $(Q_S, Q_\Omega)$ , compared to the one detected using the feature space  $E$ . For the case of the cylinder at  $Re = 3900$ , the  $\frac{R_S}{\max(R_S)}$  values increase by a factor of  $10^2$  as shown in figures 12c and 12d.

### 3.3.3. Feature space $(R_S, Q_\Omega)$

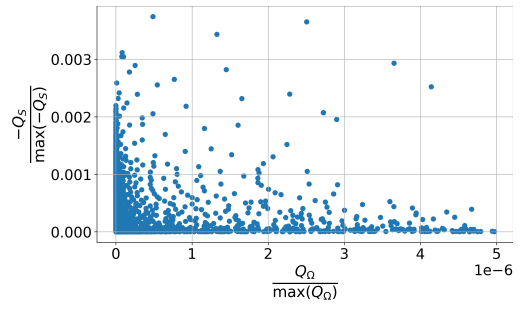
Performing the GMM clustering using  $(R_S, Q_\Omega)$  leads to the results reported in figure 13 for both laminar and turbulent cases.

The regions obtained using  $(R_S, Q_\Omega)$  in figure 13 are similar to the regions obtained from the GMM with feature space  $E$ . However, as shown in figure 14, the scatter plot of  $(-Q_S, Q_\Omega)$  shows that in the detected outer flow region the value of  $\frac{-Q_S}{\max(-Q_S)}$  increased by a factor of  $10^2$  when using  $(R_S, Q_\Omega)$  to cluster the data compared to the results obtained using the feature space  $E$ . Similar conclusions can be observed for the turbulent test case, see figures 14c and 14d.

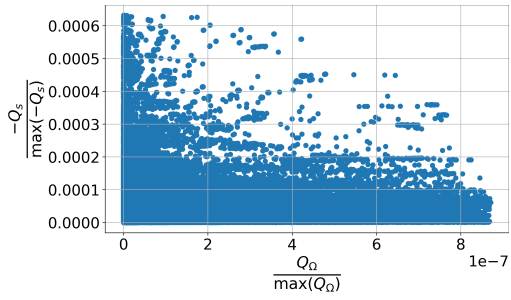
We conclude that the proposed feature space  $E = (Q_S, R_S, Q_\Omega)$  is the most robust of all the test spaces to detect laminar and turbulent regions dominated by viscosity, vorticity and turbulence, allowing a distinction from the outer inviscid (or potential) flow.



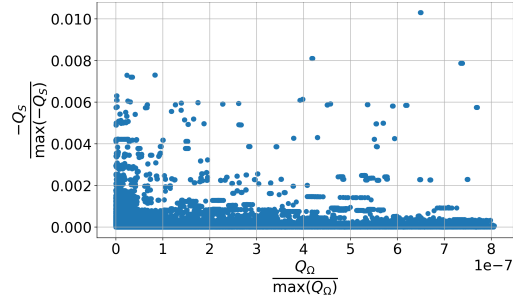
(a)  $(Q_\Omega, -Q_S)$  scatter plot in the detected outer flow region at  $Re = 40$  with feature space  $E$ .



(b)  $(Q_\Omega, -Q_S)$  scatter plot in the detected outer flow region at  $Re = 40$  with  $(R_S, Q_\Omega)$ .



(c)  $(Q_\Omega, -Q_S)$  scatter plot in the detected outer flow region at  $Re = 3900$  with feature space  $E$ .



(d)  $(Q_\Omega, -Q_S)$  scatter plot in the detected outer flow region at  $Re = 3900$  with  $(R_S, Q_\Omega)$ .

Figure 14:  $(Q_\Omega, -Q_S)$  scatter plot in the detected outer flow region by GMM using the feature space  $E$  and  $(R_S, Q_\Omega)$ .

## 4. Conclusions

We have proposed a robust clustering machine learning algorithm to distinguish viscous/turbulent dominated regions from inviscid/irrotational regions. The same feature space composed by Galilean invariants (two strain rate tensor and one rotational tensor invariant) is shown to be effective for clustering in laminar and turbulent regimes. Clustering can provide improved results compared to those of classic sensors. However, classic sensors require the tuning of parameters with arbitrary thresholds, whilst clustering is parameter-free.

In future work, the regions characterised as viscous/turbulent will be used for local mesh adaptation, where the resolution will be increased in the regions of interest to enhance local accuracy while reducing the computational cost.

## Acknowledgements

Gerasimos Ntoukas and Esteban Ferrer would like to thank the European Union's Horizon 2020 Research and Innovation Program under the Marie Skłodowska-Curie grant agreement No 813605 for the ASIMIA ITN-EID project. Additionally, the authors gratefully acknowledge the Universidad Politécnica de Madrid ([www.upm.es](http://www.upm.es)) for providing computing resources on Magerit Supercomputer.

## References

- [1] L. Alzubaidi, J. Zhang, A. J. Humaidi, A. Al-dujaili, Y. Duan, O. Al-Shamma, J. Santamaría, M. A. Fadhel, M. Al-Amidie, and L. Farhan. Review of deep learning: concepts, cnn architectures, challenges, applications, future directions. *Journal of Big Data*, 8, 2021.
- [2] Y. Bar-Sinai, S. Hoyer, J. Hickey, and M. P. Brenner. Learning data-driven discretizations for partial differential equations. *Proceedings of the National Academy of Sciences*, 116(31):15344–15349, 2019.
- [3] F. Bassi and S. Rebay. A high-order accurate discontinuous finite element method for the numerical solution of the compressible navier–stokes equations. *Journal of computational physics*, 131(2):267–279, 1997.
- [4] A. D. Beck, J. Zeifang, A. Schwarz, and D. G. Flad. A neural network based shock detection and localization approach for discontinuous galerkin methods. *Journal of Computational Physics*, 423:109824, 2020.
- [5] C. M. Bishop. *Pattern Recognition and Machine Learning*. Number 1613-9011 in Information Science and Statistics. Springer New York, NY, 1 edition, 2006.
- [6] S. L. Brunton, B. R. Noack, and P. Koumoutsakos. Machine learning for fluid mechanics. *Annual Review of Fluid Mechanics*, 52(1):477–508, 2020.
- [7] J. Callaham, J. Koch, B. Brunton, J. Kutz, and S. Brunton. Learning dominant physical processes with data-driven balance models. *Nature Communications*, 12, 02 2021.
- [8] B. Colvert, M. Alsalman, and E. Kanso. Classifying vortex wakes using neural networks. *Bioinspiration & Biomimetics*, 13, 09 2017.
- [9] C. B. da Silva and J. C. F. Pereira. Invariants of the velocity-gradient, rate-of-strain, and rate-of-rotation tensors across the turbulent/nonturbulent interface in jets. *Physics of Fluids*, 20(5):055101, 2008.
- [10] A. P. Dempster, N. M. Laird, and D. B. Rubin. Maximum likelihood from incomplete data via the em algorithm. *Journal of the Royal Statistical Society: Series B (Methodological)*, 39(1):1–22, 1977.
- [11] Ferrer, Rubio, Ntoukas, Laskowski, Marino, Colombo, Mateo-Gabin, M. de Lara, Huergo, Manzanero, Rueda-Ramirez, Kopriva, and Valero. Horses3d: a high-order discontinuous galerkin solver for flow simulations and multi-physics applications. *under review*, 2022.
- [12] E. Ferrer. An interior penalty stabilised incompressible discontinuous galerkin–fourier solver for implicit large eddy simulations. *Journal of Computational Physics*, 348:754–775, 2017.

- [13] M. Frank, D. Drikakis, and V. Charissis. Machine-learning methods for computational science and engineering. *Computation*, 8(15), 2020.
- [14] N. D. Geneva and N. Zabarar. Quantifying model form uncertainty in reynolds-averaged turbulence models with bayesian deep neural networks. *J. Comput. Phys.*, 383:125–147, 2019.
- [15] K. Horiuti and Y. Takagi. Identification method for vortex sheet structures in turbulent flows. *Physics of Fluids*, 17(12):121703, 2005.
- [16] T. Kohonen. The self-organizing map. *Proceedings of the IEEE*, 78(9):1464–1480, 1990.
- [17] M. Lanzetta, B. Mele, and R. Tognaccini. Advances in aerodynamic drag extraction by far-field methods. *Journal of Aircraft*, 52(6):1873–1886, 2015.
- [18] B. Li, Z. Yang, X. Zhang, G. He, B. Deng, and L. Shen. Using machine learning to detect the turbulent region in flow past a circular cylinder. *Journal of Fluid Mechanics*, 905, 2020.
- [19] J. Ling, A. Kurzwski, and J. Templeton. Reynolds averaged turbulence modelling using deep neural networks with embedded invariance. *Journal of Fluid Mechanics*, 807:155–166, 2016.
- [20] L. Lourenco. Characteristics of the plate turbulent near wake of a circular cylinder. a particle image velocimetry study. *In Unpublished, results taken from Beaudan and Moin*, 1994.
- [21] X. Ma, G.-S. Karamanos, and G. Karniadakis. Dynamics and low-dimensionality of a turbulent near wake. *Journal of fluid mechanics*, 410:29–65, 2000.
- [22] F. Manrique de Lara and E. Ferrer. Accelerating high order discontinuous galerkin solvers using neural networks: 1d burgers’ equation. *Computers & Fluids*, 235:105274, 03 2022.
- [23] F. Manrique de Lara and E. Ferrer. Accelerating high order discontinuous galerkin solvers using neural networks: 3d navier-stokes. *Under review*, 2022.
- [24] R. Maulik, H. Sharma, S. Patel, B. Lusch, and E. Jennings. Accelerating rans turbulence modeling using potential flow and machine learning. *arXiv: Fluid Dynamics*, 2019.
- [25] G. J. McLachlan, S. X. Lee, and S. I. Rathnayake. Finite mixture models. *Annual Review of Statistics and Its Application*, 6(1):355–378, 2019.
- [26] L. Papparone and R. Tognaccini. Computational fluid dynamics-based drag prediction and decomposition. *AIAA Journal*, 41:1647–1657, 09 2003.
- [27] P. Parnaudeau, J. Carlier, D. Heitz, and E. Lamballais. Experimental and numerical studies of the flow over a circular cylinder at reynolds number 3900. *Physics of Fluids*, 20(8):085101, 2008.

- [28] E. Patel and D. Kushwaha. Clustering cloud workloads: K-means vs gaussian mixture model. *Procedia Computer Science*, 171:158–167, 01 2020.
- [29] F. Pedregosa, G. Varoquaux, A. Gramfort, V. Michel, B. Thirion, O. Grisel, M. Blondel, G. Louppe, P. Prettenhofer, R. Weiss, R. J. Weiss, J. Vanderplas, A. Passos, D. Cournapeau, M. Brucher, M. Perrot, and E. Duchesnay. Scikit-learn: Machine learning in python. *J. Mach. Learn. Res.*, 12:2825–2830, 2011.
- [30] S. Pirozzoli. Generalized conservative approximations of split convective derivative operators. *Journal of Computational Physics*, 229(19):7180–7190, 2010.
- [31] M. Raissi, P. Perdikaris, and G. Karniadakis. Physics-informed neural networks: A deep learning framework for solving forward and inverse problems involving nonlinear partial differential equations. *Journal of Computational Physics*, 378:686–707, 2019.
- [32] R. Ranade, C. Hill, and J. Pathak. Discretizationnet: A machine-learning based solver for navier-stokes equations using finite volume discretization. *ArXiv*, abs/2005.08357, 2021.
- [33] P. L. Roe. Approximate riemann solvers, parameter vectors, and difference schemes. *Journal of computational physics*, 43(2):357–372, 1981.
- [34] A. M. Rueda-Ramirez, E. Ferrer, D. A. Kopriva, G. Rubio, and E. Valero. A statically condensed discontinuous galerkin spectral element method on gauss-lobatto nodes for the compressible navier-stokes equations. *J. Comput. Phys.*, 426:109953, 2021.
- [35] E. Saetta and R. Tognaccini. Identification of flow field regions by machine learning. *AIAA SCITECH 2022 Forum*, 2022.
- [36] A. Saxena, M. Prasad, A. Gupta, N. Bharill, O. P. Patel, A. Tiwari, M. J. Er, W. Ding, and C.-T. Lin. A review of clustering techniques and developments. *Neurocomputing*, 267:664–681, 2017.
- [37] H. Schlichting and K. Gersten. *Boundary-Layer Theory*. Springer Berlin, Heidelberg, 9 edition, 2017.
- [38] J. Sirignano and K. Spiliopoulos. Dgm: A deep learning algorithm for solving partial differential equations. *Journal of Computational Physics*, 375:1339–1364, 2018.
- [39] J. Smagorinsky. General circulation experiments with the primitive equations: I. the basic experiment. *Monthly Weather Review*, 91(3):99 – 164, 1963.
- [40] A. A. Soofi and A. Awan. Classification techniques in machine learning: Applications and issues. *Journal of Basic Applied Sciences*, 13:459–465, Jan. 2017.
- [41] B. D. Tracey, K. Duraisamy, and J. J. Alonso. A machine learning strategy to assist turbulence model development. In *53rd AIAA Aerospace Sciences Meeting*, 2015.
- [42] R. Vinuesa and S. L. Brunton. The potential of machine learning to enhance computational fluid dynamics, 2021.

- [43] E. Weinan and T. Yu. The deep ritz method: A deep learning-based numerical algorithm for solving variational problems. *Communications in Mathematics and Statistics*, 6:1–12, 2017.
- [44] J. Williamson. Low-storage runge-kutta schemes. *Journal of Computational Physics*, 35(1):48–56, 1980.
- [45] Z. Wu, J. Lee, C. Meneveau, and T. Zaki. Application of a self-organizing map to identify the turbulent-boundary-layer interface in a transitional flow. *Phys. Rev. Fluids*, 4:023902, Feb 2019.
- [46] Y. Zhou, K. Nagata, Y. Sakai, Y. Ito, and T. Hayase. On the evolution of the invariants of the velocity gradient tensor in single-square-grid-generated turbulence. *Physics of Fluids*, 27(7):075107, 2015.
- [47] L. Zhu, W. Zhang, J. Kou, and Y. Liu. Machine learning methods for turbulence modeling in subsonic flows around airfoils. *Physics of Fluids*, 31(1):015105, 2019.